ADVANCED ENERGY MATERIALS
www.advenergymat.de

Unveiling the Impact of C_{60}–O_2 Interaction on the Performance and Characterization of Perovskite Solar Cells

*Lea Zimmermann, Dorothee Menzel, Richard Gundermann, Maxim Simmonds, Florian Scheler, Thomas Gries, Edgar Nandayapa, Andres Felipe Castro Mendez, Florian Mathies, Aleksandra Miaskiewicz, Emil J. W. List-Kratochvil, Philippe Holzhey, Artem Musiienko, Felix Lang, Lars Korte, Eike Köhnen, and Steve Albrecht**

C_{60} is the prevalent electron-transport layer (ETL) in high-efficiency p-i-n perovskite single-junction and multi-junction solar cells. Here, it is demonstrated that the exposure of the C_{60} ETL to ambient O_2 results in significantly increased non-radiative recombination, influencing results from commonly applied characterization techniques such as steady-state and transient photoluminescence (PL), transient surface photovoltage, as well as current density-voltage measurements. Based on PL and He-I UV photoemission spectroscopy measurements and supported by density functional theory calculations and drift-diffusion simulations, it is proposed that O_2 rapidly intercalates into the C_{60} ETL, causing the formation of deep trap states and an altered charge carrier balance at the perovskite/C_{60} interface. The findings reveal that the effect is reversible but can mislead experimental interpretations if disregarded, emphasizing the importance of O_2 management during device fabrication and characterization. Furthermore, it is demonstrated that this interaction enables simple PL measurements in air to serve as a novel sensing method for evaluating the barrier layer quality of the SnO_x buffer layer atop C_{60}. This study thereby not only highlights a critical deterioration mechanism in perovskite solar cells and provides a deeper understanding of the underlying interaction between the C_{60} ETL and O_2 but also offers practical avenues for future selective contact optimizations.

1. Introduction

Buckminsterfullerene, C_{60}, is the predominant electron-transport layer (ETL) in high-efficiency p-i-n perovskite single-junction and multi-junction solar cells[1–12] due to its ability to rapidly extract electrons from the perovskite absorber[13,14] and its suitability for deposition via thermal evaporation, facilitating the formation of thin conformal layers.[15] However, the interface between the perovskite absorber and C_{60} also introduces significant non-radiative recombination losses, which limit the devices' open-circuit voltage (V_{OC}). This recombination predominantly takes place across the perovskite/C_{60} interface[16] and is facilitated by an unfavorable energetic alignment between the perovskite conduction band minimum (CBM) and the C_{60} lowest unoccupied molecular orbital (LUMO), along with a high density of in-gap states.[17] To address this issue, recent research efforts

L. Zimmermann, D. Menzel, M. Simmonds, F. Scheler, T. Gries, E. Nandayapa, F. Mathies, A. Miaskiewicz, E. J. W. List-Kratochvil, P. Holzhey, A. Musiienko, L. Korte, E. Köhnen, S. Albrecht
Solar Energy Division
Helmholtz-Zentrum Berlin
12489 Berlin, Germany
E-mail: steve.albrecht@helmholtz-berlin.de

The ORCID identification number(s) for the author(s) of this article can be found under https://doi.org/10.1002/aenm.202501225

DOI: 10.1002/aenm.202501225

R. Gundermann, A. F. Castro Mendez, F. Lang
Soft Matter Physics and Optoelectronics
Universität Potsdam
14476 Potsdam-Golm, Germany

E. J. W. List-Kratochvil
Department of Chemistry
Department of Physics and Center for the Science of Materials Berlin
Humboldt-Universität zu Berlin
12489 Berlin, Germany

S. Albrecht
Fakultät IV – Elektrotechnik und Informatik
Technische Universität Berlin
10587 Berlin, Germany

have focused on developing strategies to reduce the C_{60}-induced losses. These strategies range from surface treatments or interlayers that chemically passivate defects at the perovskite/ETL interface[7,18,19] or improve the interfacial energetics,[2,20–23] to the formation of so-called two-dimensional (2D) perovskite layers on top of the 3D perovskite absorber,[24,25] and the incorporation of thin spacer- or tunneling layers.[26–28]

While strategies to address non-radiative recombination losses at the perovskite/C_{60} interface have been widely explored, C_{60} as ETL holds another potential risk that so far has received only limited attention in the perovskite community: the interaction of C_{60} with oxygen (O_2). C_{60} is an excellent singlet oxygen sensitizer, i.e., photoexcited C_{60} returns to its ground state by transferring energy to molecular oxygen ($^3O_2$), generating highly reactive singlet-oxygen ($^1O_2$).[29–31] For C_{60} in various solvent environments under the presence of an electron donor and under illumination, it has further been reported that the electron transfer from C_{60} radical anions (C_{60}^-) to O_2 can result in the formation of superoxide (O_2^-).[32–34] Especially from its applications in organic solar cells and field-effect transistors, the interaction between C_{60} and O_2 is known to severely impact the electronic properties of the fullerene film, deteriorating the function of these devices.[35–38] Besides the potential photodegradation mentioned above, this is ascribed to the formation of C_{60}–O_2 dipoles[37] and/or the adsorption of molecular oxygen on C_{60}. The latter results in the formation of additional electronic states in the C_{60} bandgap and a concomitant reduction of carrier lifetime and carrier mobility.[35,36,38–42] Recently, a decline in device performance parameters due to interactions between C_{60} and O_2 was also reported for perovskite-based solar cells.[15,43] However, a detailed mechanistic study on how O_2 exposure of the C_{60} ETL affects perovskite solar cells is, to our knowledge, still lacking.

Although most fabrication and characterization steps for perovskite solar cells are typically carried out under inert conditions, exposure to ambient air and thus O_2 can occur during routine processes such as sample transfer between gloveboxes, loading into deposition chambers (e.g., for atomic layer deposition (ALD) or sputter deposition), or during characterization. Although transfer-related exposure can be avoided using sealed sample containers, preventing air contact during sample loading and characterization requires advanced infrastructure—such as glovebox-integrated deposition chambers and characterization setups. These practical limitations highlight the importance of investigating how C_{60}–O_2 interactions influence the characterization and performance of perovskite solar cells, and whether such sensitivity should be taken into account in experimental workflows and laboratory design.

In this work, we systematically investigate the interaction of the C_{60} ETL with ambient air and O_2 on state-of-the-art p-i-n perovskite solar cells, combining optoelectronic measurements and theoretical modeling. We find that the exposure of the C_{60} ETL to air results in increased non-radiative recombination in solar cell partial stacks as evidenced by steady-state photoluminescence (PL), transient PL (trPL), and transient surface photovoltage (trSPV) measurements. Furthermore, it temporarily impairs the performance of complete devices. By performing PL measurements on air- and O_2-treated solar cell partial stacks with C_{60} ETL, we can pinpoint the interaction between ambient O_2 and C_{60} as the primary culprit. Based on these results in combination with He–I ultra-violet photoemission spectroscopy (He-UPS), we propose that O_2 diffuses into the C_{60} ETL, resulting in the formation of deep trap states and altered energetics at the perovskite/C_{60} interface, thus increasing non-radiative recombination. Density functional theory (DFT) calculations and drift-diffusion simulations indicate that this trap state could correspond directly to the LUMO of O_2. Additionally, we find that based on this effect, simple PL measurements in air can be leveraged as a novel tool to assess the coverage of the SnO_x layer on top of C_{60}, thereby facilitating further optimization of this critical buffer and barrier layer for multi-junction solar cells.

2. Results and Discussion

2.1. Impact of Air Exposure on Optoelectronic Properties

To examine the impact of environmental conditions on the optoelectronic properties of inverted perovskite solar cell partial stacks after different processing steps, we performed a layer-by-layer steady-state PL analysis in nitrogen (N_2) atmosphere and air on three variations of a layer stack consisting of (1) glass/indium tin oxide (ITO)/[4-(3,6-dimethyl-9H-carbazol-9-yl)butyl]phosphonic acid (Me-4PACz) self-assembled monolayer (SAM)/1.68 eV triple-cation triple-halide (3Hal) perovskite ($Cs_{0.22}FA_{0.78}Pb(I_{0.85}Br_{0.15})_3$ + 5% $MAPbCl_3$) with no further surface treatment or ETL, (2) the same stack with a piperazinium iodide (PI) surface treatment,[2,44] and (3) with PI and an additional 18 nm C_{60} ETL on top. We have previously shown that perovskite/silicon tandem solar cells based on this layer stack as the top cell can achieve an efficiency of 32.5 %.[2] In the first step, PL measurements were performed in a N_2 atmosphere. Prior to these measurements, stringent measures were taken to ensure that samples were not exposed to air. We find that although the quasi-Fermi level splitting (QFLS, also called implied V_{OC}) is slightly reduced when PI and PI/C_{60} are deposited on the perovskite, the differences in the median QFLS values between all three sample types lie below 20 meV (see **Figure 1a**), indicating almost no PL quenching through the additional PI treatment and the subsequent C_{60} deposition, in accordance with our previous findings.[2] Conducting PL measurements on the same samples in ambient air revealed similar QFLS values to those measured in N_2 for the partial stacks without C_{60} ETL (median difference in QFLS between N_2 and air <15 meV). The slight QFLS increase in samples consisting of glass/ITO/SAM/perovskite in air contrasts reports of PL quenching upon exposure to constituents of air[45] but aligns with studies suggesting a perovskite surface passivation effect by ambient O_2.[46–48] For the solar cell partial stacks with C_{60} ETL (glass/ITO/SAM/perovskite/PI/C_{60}), however, we observed a reduction in QFLS of over 70 meV when the measurement was performed in air, which implies a drastic increase in non-radiative recombination. We found that this reduction in the QFLS occurs within the first 90 s upon air exposure and does not change with longer exposure time (see Figure S1, Supporting Information), indicating a fast and self-limiting deterioration process.

We applied the same measurement procedure on glass–glass encapsulated samples. This revealed no significant differences in the QFLS between measurements in air and N_2 for all three sample types (see Figure S2, Supporting Information)

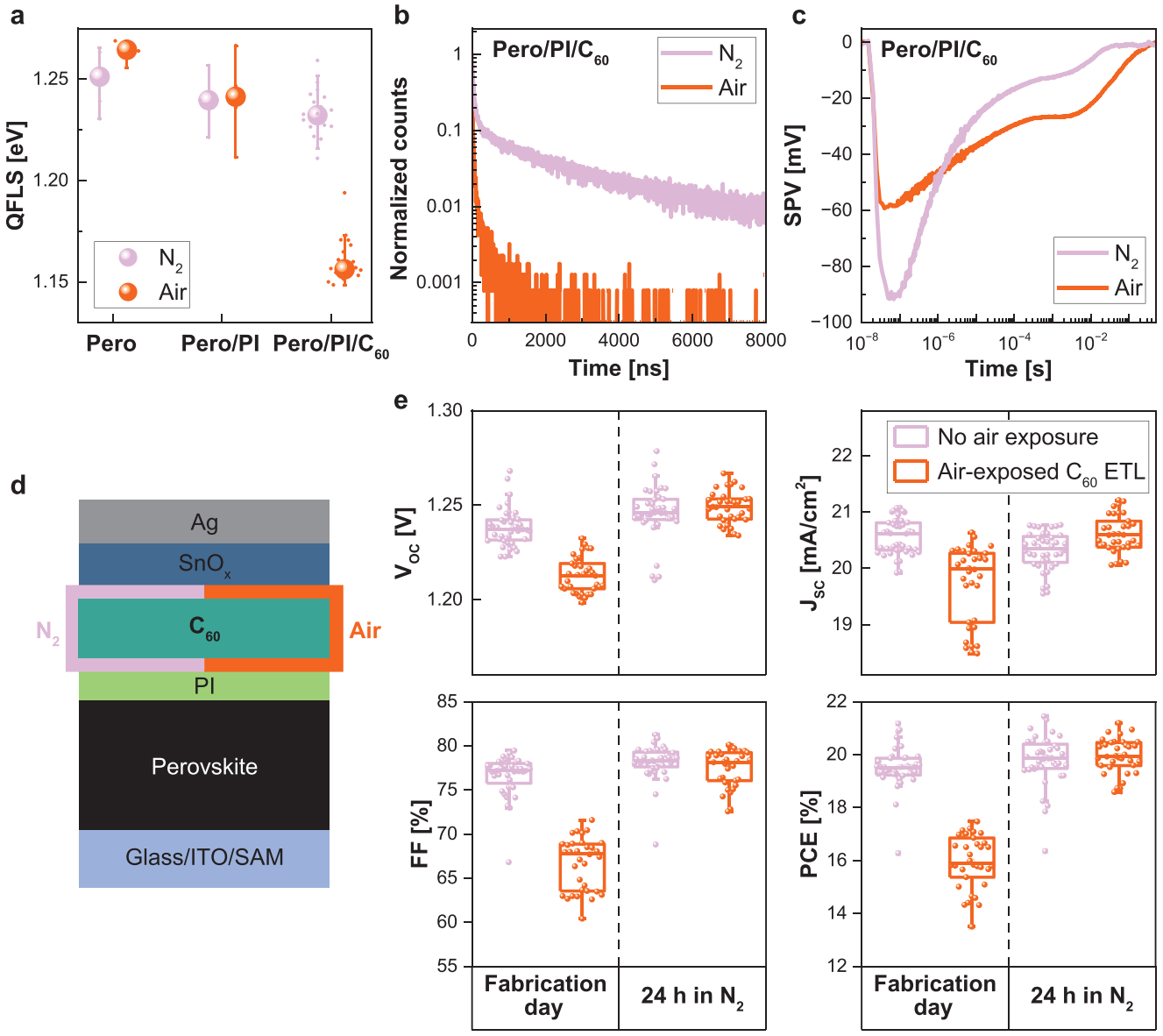

Figure 1. Impact of air exposure of C_{60} ETL on optoelectronic properties. a) QFLS of solar cell partial stacks on glass/ITO/Me-4PACz SAM were measured first in N_2 atmosphere and subsequently in ambient air. b) trPL and c) trSPV decay of air-exposed and non-air-exposed (N_2) solar cell partial stacks (glass/perovskite/PI/C_{60}). d) Schematic of the p-i-n solar cell device stack. e) Statistical representation of the V_{OC}, J_{SC}, FF, and PCE of p-i-n solar cells with a C_{60} ETL that was exposed to ambient air during the device fabrication, and of devices without air exposure. The respective *J–V* measurements were conducted on the day of fabrication (Fabrication day) and repeated after 24 h of storage in N_2 (24 h in N_2). The duration of air exposure was less than 20 min for all experiments.

demonstrating that the drop in QFLS of samples with C_{60} in air is indeed not an artefact caused by the different setups that were used for measurements in air and N_2, but a consequence of the exposure to air. Additionally, a similar QFLS reduction of samples with C_{60} in air was observed when other perovskite compositions (1.68 eV triple-cation double-halide and 1.64 eV double-halide double-cation) as well as other commonly used surface treatments and passivation strategies (lithium fluoride (LiF)[26] and/or 1,3-propanediammonium iodide (PDAI)[3,21]) were applied for passivating the perovskite/C_{60} interface (see Figure S3a, Supporting Information). Analogous to the results shown in Figure 1a such quenching behavior was not observed for the same layer stacks without C_{60} ETL (see Figure S3b, Supporting Information). This illustrates that the observed QFLS reduction in solar cell partial stacks with C_{60} as top layer in air is not specific to the 3Hal perovskite composition and the applied PI surface treatment, but rather related to the C_{60} ETL in general. Notably, the decline in QFLS upon air exposure is more pronounced for samples with higher initial QFLS values in inert atmosphere and does not occur consistently for samples without interface treatments. A higher-quality

interface, therefore, appears more sensitive to these changes or, in different terms, allows for observing this effect with higher sensitivity.

In the next step, we performed trPL and trSPV measurements on samples consisting of glass/perovskite/PI/C_{60}. Figure 1b,c shows PL and SPV transients of air-exposed and non-air-exposed samples, respectively. The air-exposed samples exhibit a significantly faster PL decay than the samples that were encapsulated in a N_2 atmosphere. We performed the same experiment on samples without interface treatment and observed a similar trend; however, with a smaller difference between air-exposed and non-air-exposed samples (see Figure S4a,b, Supporting Information). This is congruent with the observation from steady-state PL measurements that indicated a more pronounced increase in non-radiative recombination for samples with an initially lower-loss perovskite/C_{60} interface. On the other hand, this result emphasizes that although it is not visible in the QFLS values from absolute PL measurements, the air exposure of samples without perovskite/C_{60} interface passivation still influences the charge carrier recombination. In trPL, a flattening of the differential lifetime-QFLS curve as observed for the air-exposed samples (see Figure S4b,d, Supporting Information) suggests that the decay is dominated by a mechanism that is only weakly dependent on the carrier density. This points toward non-radiative recombination via deep trap states.[49,50]

The fast initial rise in the negative SPV signal for both the air-exposed and non-air-exposed samples after excitation with a 688 nm laser (Figure 1c) indicates a similarly fast extraction of electrons from the perovskite into the C_{60} ETL. The air-exposed sample, however, shows a significantly reduced SPV amplitude compared to the non-air-exposed samples by over 30 mV. This points toward a reduced absolute number of separated charge carriers. From ultraviolet–visible (UV–Vis) spectroscopy, we exclude that the lower SPV signal results from a lower absorption and, thus, a lower number of generated charge carriers in the first place (see Figure S5, Supporting Information). Accordingly, the trSPV results suggest increased trap density and/or reduced surface band bending[51] due to the exposure of the solar cell partial stack with C_{60} to air, both of which result in increased non-radiative recombination of charge carriers, consistent with the observations from steady-state and transient PL measurements.

We additionally studied the impact of air exposure on solar cell partial stacks with C_{60} using trSPV at high illumination intensities (charge carrier densities equivalent to >100 Suns, see Note S1 and Figure S6, Supporting Information). Our findings indicate that charge carrier generation and recombination within the C_{60} ETL could be significant contributors to the SPV transient under these conditions and that these processes are strongly influenced by the exposure of the partial stacks to ambient air. We further hypothesize that these effects may also account for the faster return of the SPV to zero after the maximum amplitude, or in other words, the less negative SPV signal at later times (10^{-5} to 0.1 s), as observed under 1-Sun illumination for the sample without air exposure compared to the air-exposed sample as depicted in Figure 1c.

To study the influence of air exposure on the performance of solar cells, we exposed unfinished devices after the C_{60}/SnO_x deposition to ambient air and compared their performance after the deposition of the silver (Ag) contact to devices of the same layer stack without air exposure (see complete device stack in Figure 1d). We thereby mimicked laboratory environments in which the transfer between fabrication steps cannot be conducted in an inert atmosphere. Since the 10 nm SnO_x layer does not form a closed film on top of C_{60}, we presume that the C_{60} ETL gets into contact with air (see Section 2.3). As shown in Figures 1e and S7 (Supporting Information), the air-exposed devices show a drastic reduction in all performance parameters in the current density–voltage (J–V) measurement recorded on the day of fabrication. Specifically, the median value of the open-circuit voltage (V_{OC}) decreased from 1.24 to 1.21 V when comparing devices without and with air exposure of the C_{60} ETL, respectively. The short-circuit current density (J_{SC}) dropped by 0.62 mA cm^{-2}, and the fill factor (FF) declined by an absolute of 9.44 %. Overall, this resulted in a 3.61 % absolute reduction in the power conversion efficiency (PCE) for solar cells with an air-exposed C_{60} ETL compared to the devices without air exposure. This is in line with the results from PL, trPL, and trSPV measurements of solar cell partial stacks, indicating higher non-radiative recombination caused by the exposure of C_{60} to air. The reduction in FF and J_{SC}, additionally, could be caused by a decrease in the conductivity of the C_{60} ETL upon air exposure, as recently reported by Kuba et al.[43] Remarkably, the air-exposed devices recover after 24 h of storage in N_2, reaching similar performance parameters as the non-air-exposed solar cells. A selected subset of these air-exposed and non-air-exposed devices further showed a congruent ageing behavior under constant illumination maximum power point (MPP) tracking, implying that the observed impairment is indeed fully reversible (see Figure S8, Supporting Information). A similar recovery behavior was also observed for the QFLS of solar cell partial stacks with C_{60} after exposure to air (see Figure S9, Supporting Information).

Notably, no performance deterioration was observed when the complete devices were exposed to air for the same duration (see Figure S10, Supporting Information). In this case, the underlying layers are protected by the 100 nm Ag contact, presumably shielding the C_{60} ETL from contact with air. However, it cannot be ruled out that upon prolonged air exposure, diffusion of O_2 and other components of air takes place through or along the edges of the Ag contact and eventually could result in similar deterioration effects as observed for the samples without Ag contact.

2.2. Mechanistic Insights

In order to gain insight into the root cause of the observed degradation, we carried out PL measurements on solar cell partial stacks (glass/ITO/SAM/perovskite/PI/C_{60}) using pure O_2 and ambient air at different pressures. This enabled us to differentiate between the effect of O_2 as one of the main components of air and other constituents of this gas mixture. As depicted in **Figure 2a**, for pure O_2, the PL signal started to decrease from an O_2 pressure of 1 mbar and eventually dropped to 12% of the initial PL emission (measured at 0.05 mbar N_2) at an O_2 pressure of 1 bar (see also Figure S11, Supporting Information). A similar trend was observed when we performed the same experiment with ambient air. However, at the same O_2 partial pressure, the PL signal was quenched less when ambient air was used instead of pure O_2. This most likely stems from minor sample-to-sample

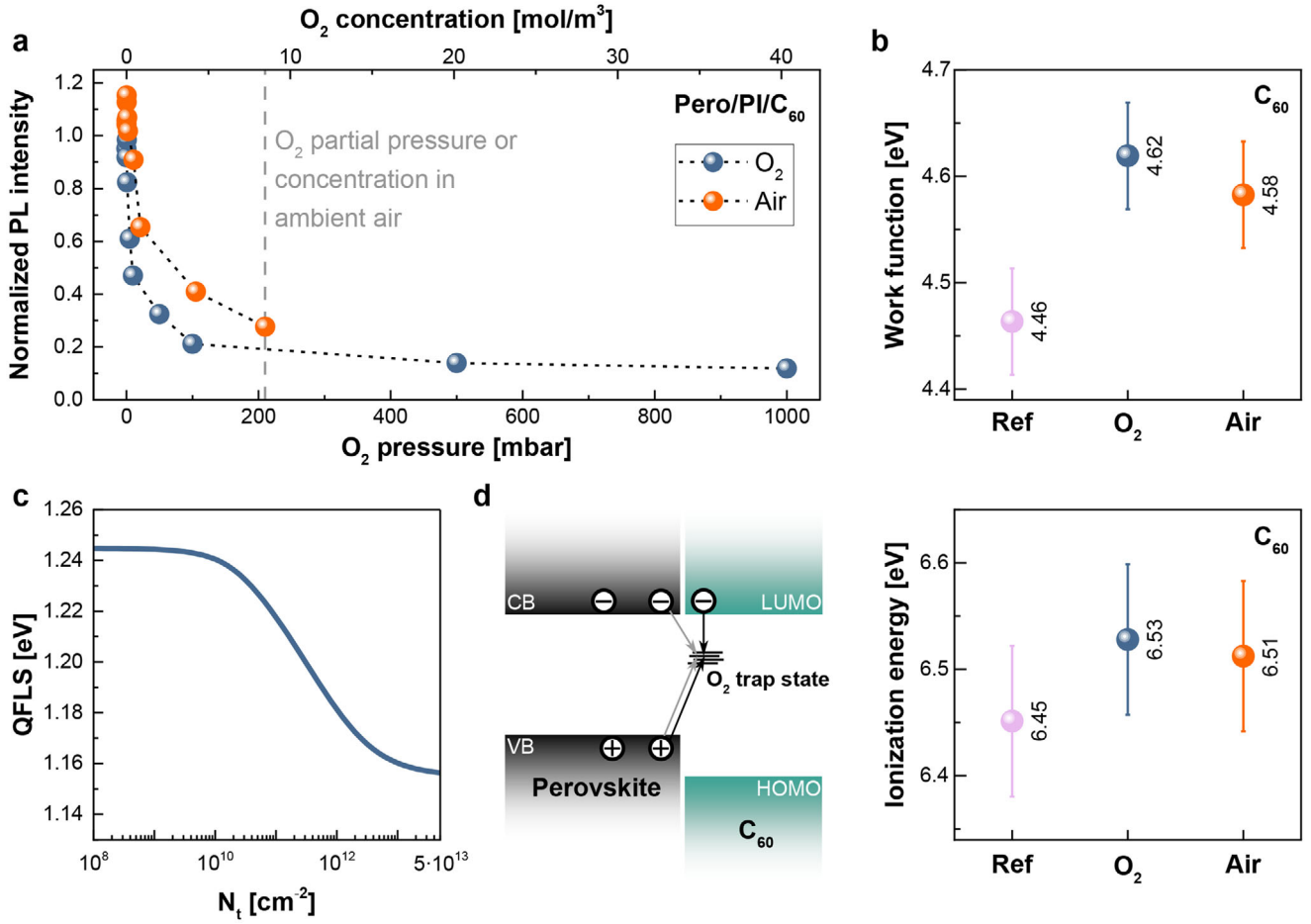

Figure 2. Mechanistic insights into C_{60}–O_2 interaction. a) Normalized PL intensity of solar cell partial stacks on glass/ITO/SAM at varying O_2 partial pressures. The measurements were performed by progressively increasing the pressure of pure O_2 or ambient air, starting from an initial pressure of 0.05 mbar. The PL intensity was normalized to the emission measured under the initial inert condition of 0.05 mbar N_2, prior to the introduction of air or O_2 into the measurement chamber. b) Work function and ionization energy of C_{60} thin films from He-UPS measurements. The reference sample (Ref) was stored in N_2 and Ar, while the O_2 and air samples were exposed to 1 bar of O_2 and air for 15 min, respectively. c) Dependence of QFLS on interface trap densities calculated by drift-diffusion modeling. The energetic position of the trap state used as the input parameter corresponds to the LUMO of O_2. d) Simplified schematic of the proposed mechanism for the C_{60}–O_2 interaction in perovskite solar cells.

variations that were also observed in the absolute PL measurements represented in Figure 1a. Other air constituents do not appear to be a source of additional quenching, indicating that O_2 in ambient air is the primary cause for the observed PL reduction.

To explicitly assess the role of H_2O, we additionally performed PL measurements on solar cell partial stacks exposed to air with varying relative humidity (RH) levels (0% to 80% RH at 25 °C, see Figure S12, Supporting Information). The decline in QFLS was very similar across all tested humidity conditions, confirming that moisture in the air within the relevant humidity range does not contribute additional PL quenching beyond that caused by dry air. Although we cannot completely exclude a potential influence of H_2O on the studied system and the C_{60} ETL, these results suggest that its effect is significantly smaller than that of O_2 under typical atmospheric conditions.

To correlate the observed effects upon O_2 and air exposure with potential changes in the electronic structure, we studied air- and O_2-treated C_{60} thin films by He-UPS. The measurements were conducted under ultra-high vacuum (UHV) conditions. We note that the observed effects of O_2 exposure are reversible. Therefore, we ensured a consistent protocol from transfer to UHV until the measurement for all samples and reduced the exposure to UHV prior to the measurements to a minimum (<20 min). Nevertheless, it is likely that exposure to UHV before the measurement partially reverses the effects of O_2, meaning that the energetic shifts observed with He-UPS, as discussed below, may not represent the full extent of energetic shifts upon O_2 exposure. As shown in Figure 2b, we observed an increase in both work function (WF) and ionization energy (IE) for the samples that had been exposed to 1 bar of O_2 or air compared to the reference that was stored in N_2 and Argon (Ar) atmosphere (see secondary electron cut-off (SECO) and highest occupied molecular orbital (HOMO) region and respective fits in Figure S13, Supporting Information). With a WF and IE shift relative to the N_2/Ar-stored reference of 160 and 80 meV, respectively, the O_2-treated sample undergoes a slightly more pronounced alteration compared to the air-exposed sample (WF and IE difference to N_2/Ar-reference of 120 and 60 meV, respectively). Accordingly, we suspect that this

shift is caused by an interaction of the C_{60} layer with O_2 and that the observed difference between the air- and O_2-exposed sample correlates with the lower O_2 concentration in air of 21%$_{mol}$. This is consistent with the above-shown PL results under different O_2 concentrations and, thereby, indicates that the change in WF and IE detected by UPS is directly related to the observed PL quenching.

We further supported these findings under conditions relevant to typical processing and characterization environments by performing Kelvin probe (KP) measurements on a C_{60} thin film identical in layout to those used for He-UPS, under 1 bar N_2, followed by 1 bar ambient air. We observed a 100 meV increase in the WF upon air exposure (see Figure S14 and Table S1, Supporting Information), closely matching the 120 meV shift observed in He-UPS measurements. This consistency confirms that the He-UPS results reliably capture the effect of air exposure, despite the potential for partial desorption under UHV conditions.

A shift of the WF can be due to either a change of the Fermi level position within the bandgap and/or the formation/change of a surface dipole. The He-UPS results demonstrate a shift of the Fermi level closer to the HOMO level of 80 and 60 meV for the O_2 and air-exposed sample, respectively. Assuming a constant bandgap energy of C_{60} for all three sample types, this indicates a reduction in n-type character through the treatment with air or O_2. This hints toward charge transfer from the C_{60} to, e.g., additional trap states, which will be discussed in more detail below. Since we also observed a shift in the IE, which is, however, significantly smaller than the WF shift, we suspect an additional formation of a positive surface dipole[52] with its absolute value given by the difference in IE between the O_2- or air-treated sample and the reference, respectively. Both the Fermi level shift and the surface dipole add up to the overall observed change in the WF.

Notably, we observed a slightly flattened SECO for the air- and O_2-treated samples (see Figure S13b,c, Supporting Information) that could be indicative of a damaged C_{60} surface. To investigate if the samples underwent chemical changes, such as the formation of $C_{60}O_x$[53–55] and/or incorporated impurities upon the O_2 and air exposure, we performed X-ray photoelectron spectroscopy (XPS) on the same samples. In the obtained spectra, we find only minor differences within the C 1s region and a generally low oxygen content (see Figure S15, Supporting Information). Only the O_2-exposed sample shows a broadened O 1s peak toward higher binding energy, indicative of a larger -OH fraction, potentially due to oxygen-induced defects on the C_{60} surface. Nevertheless, since there is no significant change either in the C 1s region or the oxygen content for the air-treated sample, we cannot directly correlate the observed WF and IE shift to a change in the surface chemical bond environment detectable by XPS. It is, however, conceivable that chemical bonds and/or impurities that cause a change in the electronic levels are also present in the air-treated C_{60} thin film, but in a concentration that is below the detection limit of XPS. Additionally, weakly adsorbed oxygen species might get partially desorbed under prolonged UHV exposure prior to the XPS measurements, which followed the UPS measurements.

Given the observed reversibility of the QFLS and *J*–*V* parameters without additional energy input following the short air exposure duration studied here (<20 min), together with the results from XPS, we do not consider the formation of new chemical bonds as a cause for the deterioration of the optoelectronic properties. This further aligns with reports indicating that irreversible changes of C_{60} occur only after prolonged exposure to O_2 and simultaneous irradiation.[53,55–57] Accordingly, we propose that weak adsorption of O_2 on/in the C_{60} layer suffices to cause the effects described above. This is supported by various reports describing the formation of deep states in the C_{60} HOMO-LUMO gap upon O_2 adsorption.[39–41,57,58] Electron transfer from C_{60} to these states allows O_2 to act as a p-type dopant,[39,57,58] which aligns well with the shift in the Fermi level observed in He-UPS measurements of O_2- and air-treated C_{60} thin films as well as with the reduced SPV amplitude of air-exposed solar cell partial stacks in our work. Additionally, the electric field generated by this charge transfer may induce polarization of the C_{60} molecules, introducing a dipole[59,60] that further shifts both the WF and IE, consistent with our experimental observations.

Assuming O_2 intercalates throughout the C_{60} ETL and to the perovskite/C_{60} interface, the deep states created by O_2 adsorption could serve as recombination centers, facilitating the non-radiative recombination of electrons with holes from the perovskite. These electrons may originate either from the perovskite absorber itself or from those already extracted into the C_{60} ETL. The extraction of both electrons and holes into and their recombination in the C_{60} ETL is considered unlikely due to the presence of a barrier for holes at the perovskite/C_{60} interface, even when accounting for hole extraction via excitonic states in the C_{60}[16] and changed energetics upon O_2 exposure as indicated by He-UPS. The observed shift of the Fermi level toward the C_{60} midgap could further impair the electron transporting properties of the ETL, and under the assumption that this effect extends to the interface with the absorber, it potentially also affects the energetic alignment and charge carrier redistribution at the perovskite/C_{60} interface. This could reduce the charge carrier selectivity, hindering efficient electron extraction and increasing the concentration of holes (minority carriers) at the interface and, thus, making the interface even more susceptible to non-radiative recombination.

To get more insight into the system of C_{60} with absorbed O_2, we performed DFT calculations of a C_{60} and O_2 molecule in a single supercell under the assumption that there are no chemical interactions between the two molecules (see detailed description in Note S2, Supporting Information). The results indicate that the LUMO of O_2 is positioned 0.57 eV below the C_{60} LUMO (see density of states (DOS) plot in Figure S16b, Supporting Information) and, consequently, below the Fermi level of O_2-free C_{60}, as measured by He-UPS. This suggests that electron transfer from C_{60} to the O_2 LUMO is likely. Accordingly, we infer that the trap state indirectly observed by He-UPS could correspond directly to the LUMO of O_2.

To further investigate whether the LUMO level of O_2 could serve as an interfacial trap state, facilitating recombination of charge carriers at or across the perovskite/C_{60} interface, we applied drift-diffusion modeling. To this end, we estimated the capture coefficients of interfacial trap states at the energetic position of the O_2 LUMO as determined by DFT calculations based on a model applied by Kirchartz et al.[61] (see Note S3, Supporting Information). This allowed us to calculate the QFLS of solar cell partial stacks with C_{60} ETL at varying densities of these interface traps (see Note S4, Supporting Information). The

results revealed that an interfacial trap state with this energetic position could indeed result in increased non-radiative recombination and a reduction in QFLS of >70 meV at trap densities greater than $2 \cdot 10^{12}$ cm^{-2} (see Figure 2c). This theoretically calculated QFLS drop closely matches our experimental observations. Furthermore, a density of "O_2 traps" of up to $5 \cdot 10^{13}$ cm^{-2} is plausible, assuming an ideal face-centered cubic (fcc) crystal structure of C_{60} at the interface with the perovskite, with O_2 molecules occupying the octahedral sites within this structure.[55,62] Although this assumption was used to estimate the interfacial O_2 concentration, the DFT calculations discussed above were performed on isolated C_{60} and O_2 molecules and did not rely on this structural model.

The proposed mechanism involving the O_2 LUMO as a deep trap in the C_{60} bandgap includes electron transfer from the perovskite CBM and/or C_{60} LUMO to the LUMO of O_2. Similarly, Hoke et al.[63] suggested electron transfer from fullerenes to gaseous O_2, resulting in the formation of superoxide anions, in the context of photobleaching in organic solar cells. Under continuous ad- and desorption of gaseous oxygen, the electron may be captured by O_2 and removed from the device, preventing the radiative recombination with a hole in the perovskite layer. This mechanism of O_2^- ions acting as an electron sink, however, is less likely for the system studied in this work. Given that the effect remains even after cutting the cell from continuous ground state O_2 supply by transferring it to an inert gas atmosphere, together with the recovery after air exposure taking several hours, this rather suggests a slow desorption and outdiffusion process. Furthermore, although probably significant for, e.g., the PL deterioration of stand-alone C_{60} thin films[64] (see also discussion in Note S5, Supporting Information), the formation of singlet-oxygen on C_{60} is believed to play an negligible role in the system discussed here, as it does not provide a mechanism for non-radiative recombination of charge carriers in the perovskite absorber. Moreover, we exclude degradation pathways involving the dissociation of O_2 molecules into atomic oxygen, as this process requires a higher energy input from heat and/or illumination than applied in this study. We further note that the effect studied in this work is different from the mechanism that was recently shown by Said et al.[15] where they demonstrated a reduced batch-to-batch reproducibility of perovskite/silicon tandem devices due to the coalescence of C_{60} molecules during repeated thermal evaporation processes caused by oxygen impurities in the source powder.

Accordingly, based on our findings, we infer that the dominant mechanism for the observed effects upon exposure of the C_{60} ETL to ambient air in PL, trPL, trSPV, and *J–V* measurements is caused by the reversible intercalation of O_2 into the C_{60} ETL and to the perovskite/C_{60} interface. This results in deep trap states in the C_{60} HOMO–LUMO gap that facilitate non-radiative recombination at and/or across the perovskite/C_{60} interface, as illustrated in Figure 2d. DFT calculations and drift-diffusion simulations indicate that this deep trap state could correspond directly to the LUMO of O_2. Additionally, the changes in the electronic properties of C_{60}, as observed by He-UPS and presumably linked to the charge transfer between C_{60} and the deep trap state caused by the adsorption of O_2, could impair the electron transporting properties of the ETL and potentially reduce carrier selectivity, increasing the concentration of minority carriers (holes) at the interface, and reducing the efficiency of electron extraction, thus posing an additional cause for increased non-radiative recombination.

To generalize our findings, we expanded our study to other commonly applied C_{60}-based electron-selective materials. We therefore replaced thermally evaporated C_{60} in solar cell partial stacks with spin-coated phenyl-C_{61}-butyric acid methyl ester (PCBM), indene-C_{60} bisadduct (ICBA), and indene-C_{60} monoadduct (ICMA), and performed PL measurements first in N_2 and subsequently in air. As depicted in Figure S18 (Supporting Information), a QFLS reduction upon air exposure was observed with all tested C_{60}-derivatives, with and without PI surface treatment. Hence, we assume that the deterioration driven by additional trap states at the perovskite/ETL interface through the exposure to ambient O_2, found for C_{60}, also occurred for the screened fullerene derivatives. Nevertheless, we observed differences in the magnitude by which the QFLS of solar cell partial stacks with different fullerene ETLs decreased upon air exposure. This observation could be related to the initially different quality of the perovskite/ETL interface, the position of the fullerenes' energetic levels, their film coverage on the perovskite absorber, as well as to the available number of interstitial sites for O_2. A more detailed discussion can be found in Note S7 (Supporting Information).

In light of a broader context, although the detrimental effects of O_2 on C_{60} discussed here are specific to fullerene-based ETLs in p-i-n architectures, it is worth noting that O_2 exposure plays a contrasting role in n-i-p devices employing spiro-OMeTAD as a hole-transport layer, where controlled oxidation can enhance hole transport properties and thereby improve the device performance.[65]

2.3. Utility as SnO_x Coverage Test

Alongside the C_{60} ETL, the commonly applied SnO_x buffer layer on top has also been subject to intense research in the perovskite community.[2,66–72] Particularly, it has been the focus of attention due to its poor growth characteristics by ALD on C_{60}-based fullerenes,[67,68,70] making it challenging to form dense and well-covering films. Good SnO_x coverage can be specifically important since the layer serves as a protection layer against sputter damage for the subsequent deposition of the transparent conductive oxide (TCO) in multi-junction devices[73] and as a barrier layer to avoid diffusion processes within the perovskite solar cell, which can deteriorate the operational stability.[69] Multiple publications addressed this issue and proposed solutions by inserting, e.g., a polymer[68] or aluminum-doped zinc oxide (AZO) nucleation layer[67,69] on top of the fullerene ETL or by introducing an intermediate ozone-treatment step into the deposition process.[70] However, in these studies, the layer quality and its coverage on the ETL are typically tested by complex measurement techniques such as XPS or scanning transmission electron microscopy (STEM), impeding an efficient and fast optimization loop. Since our experimental results indicate that suitable solar cell partial stacks with C_{60} are highly sensitive to the ingress of ambient O_2, we propose that the interaction between the C_{60} ETL and ambient O_2 can be leveraged to probe the SnO_x coverage on top of the stack and thereby facilitate further optimizations. To verify the viability of this approach, we performed PL

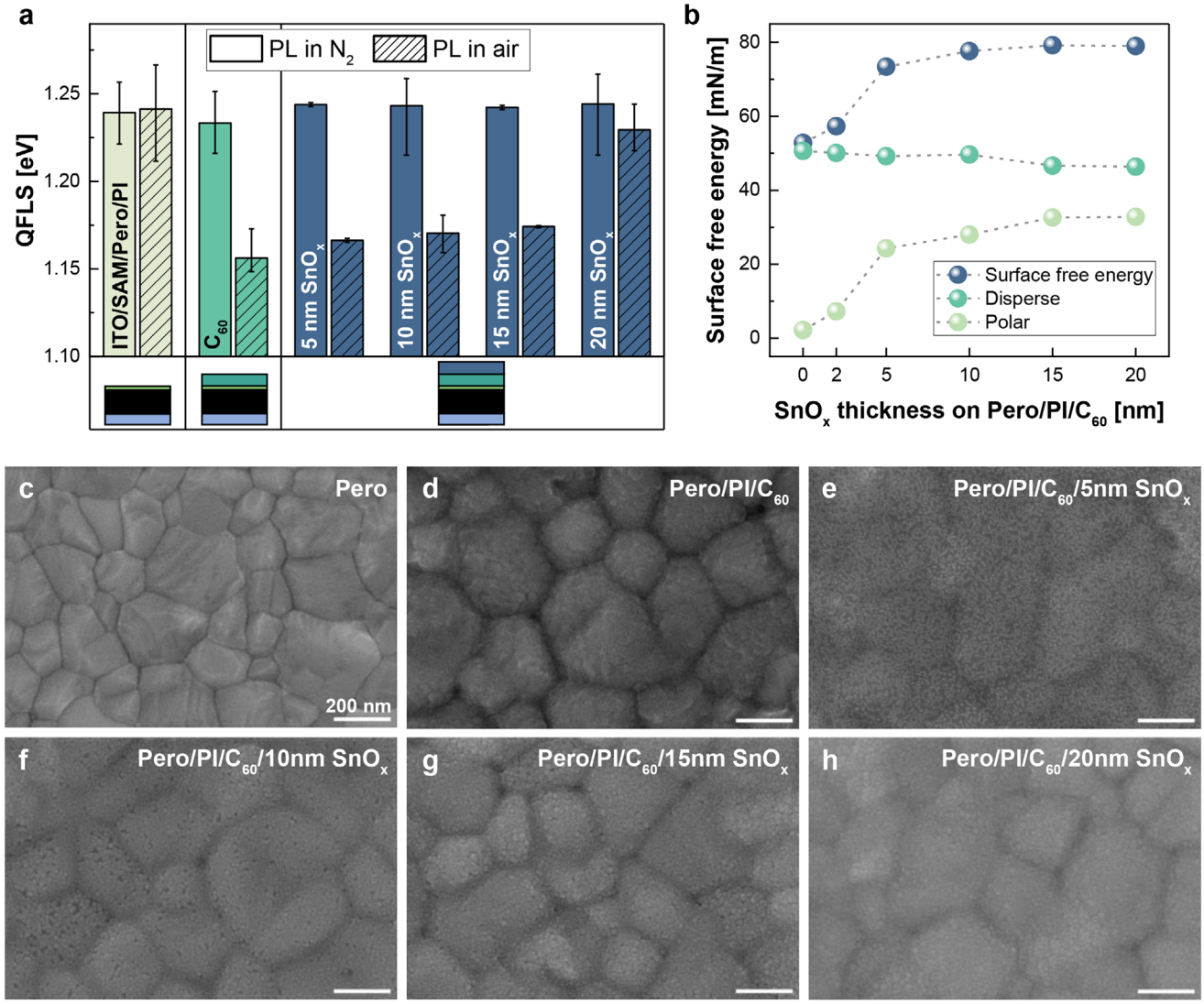

Figure 3. PL in air as SnO_x coverage test. a) QFLS obtained by PL measurements of solar cell partial stacks glass/ITO/SAM/perovskite/PI, with C_{60}, and incremental SnO_x buffer layer thicknesses in N_2 and air. b) Surface free energy, and respective disperse and polar parts of glass/ITO/SAM/perovskite/PI/C_{60}/SnO_x with different SnO_x thicknesses. c–h) SEM images of the perovskite surface, the latter covered with PI/C_{60}, and SnO_x layer thicknesses of 5, 10, 15, and 20 nm, respectively.

measurements of solar cell partial stacks with C_{60} and SnO_x layers of thicknesses between 5 and 20 nm in N_2 and air. As shown in **Figure 3a**, at SnO_x layer thicknesses below 20 nm, we observe a similar QFLS drop upon air exposure as for the samples without SnO_x, whereas at a thickness of 20 nm, we obtain very similar QFLS in air and N_2 atmosphere. These findings imply that for SnO_x thicknesses between 5 and 15 nm, the underlying C_{60} ETL was exposed to air, causing increased non-radiative recombination via the mechanism described above, and thus indicating a non-closed SnO_x layer for the tested thicknesses below 20 nm. At a layer thickness of 20 nm, however, it is inferred that a sufficient encapsulation effect is achieved, preventing the exposure of the C_{60} ETL to ambient O_2.

This deduction is further validated by contact angle measurements (CAM) on solar cell partial stacks with different SnO_x thicknesses. For these measurements, small volumes of a liquid are dropped onto a solid surface. Based on the angle between the tangent to the liquid-vapor interface of polar and dispersive liquids and the sample surface, the surface free energy can be calculated.[74,75] The results from measurements with water and diiodo-methane reveal an increase in the surface free energy with increasing SnO_x thickness, eventually reaching a plateau at 15 nm (Figure 3b and Figure S20 and Table S7, Supporting Information). This trend represents the progressive masking of the predominantly hydrophobic characteristic of C_{60} by the hydrophilic SnO_x with increasing layer thickness and supports a SnO_x full-coverage threshold at approximately 15 nm.

We additionally obtained SEM images of solar cell partial stacks of the bare perovskite, the latter topped with 18 nm C_{60} and SnO_x layers with thicknesses between 5 and 20 nm (Figure 3c–h). The images reveal clear island growth of SnO_x on C_{60} and display a closed layer at a thickness of 20 nm. This agrees well with the

results from PL measurements on solar cell partial stacks, thereby confirming this simple method as a valid technique to assess the SnO_x coverage. It further highlights the excellent sensitivity of this method. Whereas at a SnO_x thickness of 15 nm, the surface free energy obtained by CAM is already completely dominated by the SnO_x properties, the PL measurements in air still show a QFLS reduction caused by the diffusion of O_2 through the few isolated holes of the nearly closed SnO_x layer as visible by SEM.

Moreover, due to its working principle being based on the C_{60} underneath, this PL-based test is not exclusive to SnO_x but can be leveraged to test the O_2-barrier layer quality of other buffer layer materials, such as bathocuproine (BCP). As shown in Figure S21 (Supporting Information), BCP did not exhibit effective suppression of O_2-induced degradation, as the QFLS decline upon air exposure was comparable to that observed in stacks without a buffer layer. These results demonstrate that this straightforward characterization method can be applied to a variety of buffer layers and may provide a useful tool for the systematic evaluation and future design of oxygen barrier materials in perovskite solar cells.

3. Conclusion

In this study, we uncovered the impact of the interaction between C_{60} and O_2 on perovskite solar cells and their characterization and proposed a mechanism for its underlying cause. Our findings demonstrate that the exposure of the C_{60} ETL to air and, thus, O_2, leads to a substantial increase in non-radiative recombination, as revealed by steady-state and transient PL as well as trSPV measurements. The temporarily impaired performance of complete perovskite solar cells featuring a C_{60} ETL exposed to air during device fabrication further underscores the practical relevance of this interaction.

To uncover the underlying mechanism, we combined experimental and theoretical approaches. Steady-state PL measurements identified O_2 as the primary cause of the observed effects, while He-UPS of C_{60} thin films revealed a shift of the Fermi level toward the C_{60} midgap and, thus, a reduction in n-type character upon air or O_2 exposure. These energetic changes could be explained by deep trap states in the C_{60} HOMO–LUMO gap caused by the adsorption of O_2. DFT calculations indicate that this deep trap state could correspond directly to the LUMO of O_2, while drift-diffusion modeling confirmed its potential role as an efficient recombination center at the perovskite/C_{60} interface. In essence, we propose that the exposure of the C_{60} ETL to (ambient) O_2 results in deep trap states and an altered charge carrier balance at the perovskite/C_{60} interface, promoting significant non-radiative recombination. This behavior was further generalized to other commonly applied fullerene derivates.

A key insight from our work is that although the interaction between C_{60} and O_2 under the studied conditions appears to be fully reversible, neglecting this interaction can significantly influence the interpretation of experimental results. This is of particular importance since laboratory environments often do not allow to completely avoid the exposure of (unfinished) samples, and with that the C_{60} ETL, to air. Our findings, therefore, highlight the importance of accounting for air exposure—through appropriate infrastructure, workflow design, and environmental controls—to ensure reproducibility in both academic and industrial perovskite solar cell development.

Although not explicitly studied in this work, it is important to note that commonly applied encapsulation strategies for long-term stability testing are often insufficient to fully protect devices or partial stack samples from ambient O_2.[76] Consequently, the effects observed in this study may also have implications for long-term stability tests. Additionally, upon standard testing conditions, illumination could further translate temporal changes of adsorption to permanent changes by photoactivated chemical reactions.[53,55–57]

We further demonstrated that ensuring full coverage of the SnO_x layer atop the C_{60} layer effectively mitigates the interaction between C_{60} and ambient O_2 by preventing direct exposure of the ETL to air. Accordingly, our findings reveal that simple PL measurements conducted in air can be employed as an efficient tool to evaluate the quality of the SnO_x barrier layer.

Our study thereby highlights the importance of O_2 management during perovskite solar cell fabrication and characterization to ensure reliable and reproducible metrics, and additionally provides practical avenues for facilitating the optimization toward effective SnO_x barrier layers.

4. Experimental Section

Materials: Anhydrous (anh.) dimethyl sulfoxide (DMSO, ≥99.99%), anh. dimethylformamide (DMF, 99.8%), anh. anisole (99.7%), anh. isopropanol (IPA, 99.5%), anh. chlorobenzene (CBZ, 99.8%), propane-1,3-diammonium iodide (PDAI, ≥98%), and lithium fluoride (LiF) were purchased from Sigma–Aldrich. Formamidinium iodide (FAI, 99.99%), methylammonium chloride (MACl, 99.99%), and methylammonium bromide (MABr, 99.99%) were purchased from Dyenamo. Lead iodide (PbI_2, 99.99%), lead bromide ($PbBr_2$, ≥98.0%), lead chloride ($PbCl_2$, >99.0%), [4-(3,6-dimethyl-9H-carbazol-9yl)butyl]phosphonic acid (Me-4PACz) and 1,6-hexylenediphosphonic acid (6dPA) were purchased from Tokyo Chemical Industry Co., Ltd. (TCI). Cesium iodide (CsI, 99.999%) was purchased from abcr GmbH. Ethanol (EtOH, anh.) was obtained from VWR. PI was synthesized by Dr. Mantione at POLYMAT. 1,2-Dichlorobenze (o-DCB, >99%) was purchased from Thermo Scientific. Fullerene C_{60} (sublimed; purity ≥99.99%) was obtained from Crea-Phys GmbH. Phenyl-C_{61}-butyric acid methyl ester (PCBM, >99.5%) was purchased from Luminescence Technology Corp. Indene-C_{60} bisadduct (ICBA) and indene-C_{60} monoadduct (ICMA) were obtained from Nano-C. Tetrakis(dimethylamino)tin(IV) (TDMASn, precursor for SnO_2, 99.99% Sn) was acquired from STREM Chemicals, Inc. Sublimed bathocuproine (BCP, sublimed, 99.5%) and silver (Ag) were ordered from Ossila and Alfa–Aesar, respectively. All the materials were used as received without any further purification.

Fabrication of Solar Cell Partial Stacks: Glass/indium tin oxide (ITO) or glass substrates were cleaned by ultra-sonication in H_2O with detergent (Hellmanex, 2%), H_2O, acetone, and IPA for 10 min each. For the hole transport layer (HTL), [4-(3,6-dimethyl-9H-carbazol-9-yl)butyl]phosphonic acid (Me-4PACz), and 1,6-hexylenediphosphonic acid (6dPA) were dissolved individually in ethanol and mixed in a 4:1 volume ratio as described in ref.[77]. The solution was then spin-coated in a nitrogen glovebox at 3000 rpm for 20 s and annealed at 100 °C for 10 min. All following spin-coating processes were also conducted in nitrogen gloveboxes.

For the 1.4M triple-cation triple-halide (3Hal) perovskite ($Cs_{0.22}FA_{0.78}Pb(I_{0.85}Br_{0.15})_3$ + 5% $MAPbCl_3$) (1.68 eV) precursor, a $Cs_{0.22}FA_{0.78}Pb(Br_{0.15}\ I_{0.85})_3$ solution was prepared in a mixture of DMF and DMSO (volume ratio DMF:DMSO 3:1) and added to the $MAPbCl_3$ solids in a second step. The solution was spin-coated at 5000 rpm for 45 s, using 5 s acceleration and 250 µL anisole as antisolvent at 25 s

from the beginning of the spin-coating process. The perovskite film was annealed at 100 °C for 20 min.

For the 1.4M triple-cation double-halide perovskite (3Cat) ($Cs_{0.05}(MA_{0.23}FA_{0.77})_{0.95}Pb(Br_{0.23}I_{0.77})_3$), all solids were dissolved in a mixture of DMF and DMSO (volume ratio 4:1). The precursor solution for the 1.64 eV double-cation double-halide (FACs) perovskite ($Cs_{0.22}FA_{0.78}Pb(I_{0.85}Br_{0.15})_3$) was prepared by dissolving the solid components in a mixture of DMF and DMSO with a volume ratio of 3:1. The spin-coating for the 3Cat and FACs perovskite was conducted in the same way as described for the 3Hal perovskite.

For the PI surface treatment, a 0.3 mg mL^{-1} solution of PI in IPA was spin-coated at 5000 rpm for 20 s and annealed for 10 min at 100 °C. After the annealing, the surface was washed by spin-coating IPA, using the same spin-coating recipe as for the PI solution, followed by 2 min annealing at 100 °C. For the PDAI interface treatment, a 1 mg mL^{-1} solution of PDAI in IPA was spin-coated at 4000 rpm for 25 s. If LiF was used as an interlayer at the perovskite/C_{60} interface, 1 nm of the material was thermally evaporated on top of the perovskite absorber.

Following the surface treatment or interlayer deposition, 18 nm C_{60} was thermally evaporated. For the tests with other fullerene derivates, the ETL was spin-coated. Therefore, 2 mg mL^{-1} ICMA or ICBA were dissolved in o-DCB, respectively, and dropped onto the perovskite absorber prior to starting the spin-coating program (5 s acceleration, 20 s at 3000 rpm). The samples were not annealed after spin-coating. PCBM was dissolved in CB with a concentration of 5 mg mL^{-1} and deposited in the same way as ICBA and ICMA.

SnO_x buffer layers were deposited by ALD in an Arradiance GEMStar reactor. TDMASn was used as the Sn precursor and was held at 60 °C in a stainless-steel container. Water was used as an oxidant and was delivered from a stainless-steel container without active heating, whereas the precursor delivery manifold was heated to 115 °C. For the deposition at 80 °C, the TDMASn/purge/H_2O/purge times were 1/10/0.2/15 s with corresponding nitrogen flows of 30/90/90/90 sccm. With this, 140, 115, 70, and 35 cycles lead to 20, 15, 10, and 5 nm SnO_x, respectively. The SnO_x thicknesses on silicon were confirmed by spectral ellipsometry.

If BCP was applied instead of SnO_x, 8 nm of the material was thermally evaporated after the deposition of C_{60} without breaking the vacuum.

Fabrication of Perovskite Solar Cells: For p-i-n perovskite solar cells, the following layer stack was used: glass/ITO/Me-4PACz/3Hal perovskite/PI/C_{60}/SnO_x/Ag. For the deposition of these layers, the same fabrication steps were conducted as described for solar cell partial stacks. As substrates, laser-patterned ITO on glass substrates were used with six independent ITO pixels confined by laser scribes (nominal ITO thickness of 150 nm, 15 Ω sq^{-1} sheet resistance, Automatic Research GmbH). The 0.16 cm^2 active area is determined by the overlap between the area confined by the laser scribe and the 4 mm broad Ag stripes (100 nm thickness) that were thermally evaporated using shadow masks. For devices with air-exposed C_{60}, the unfinished devices were exposed to ambient air for 15 min after the SnO_x deposition and before the Ag contact was deposited.

Encapsulation: For steady-state PL measurements of solar cell partial stack samples, the glass or glass/ITO substrate served as one side of the glass-glass encapsulation, while a cavity glass (borosilicate glass, AMG, Korea) was used on the opposite side. The edges were sealed by UV glue (Blufixx).

For transient PL (trPL) and transient surface photovoltage (trSPV) measurements, a similar encapsulation strategy was applied. Instead of cavity glasses thinner cover glasses (P. Marienfeld GmbH, 0.16–0.19 mm thickness) were used. To keep the samples optically comparable, both air- and non-air-exposed samples were encapsulated. The non-air-exposed samples were encapsulated in N_2 atmosphere. For the air-exposed samples, the encapsulation was performed before the measurement in ambient air.

Photoluminescence: In this work, four different setups for absolute PL measurements were used.

Setup 1: For absolute PL measurements of solar cell partial stacks in air, a home-built setup was used where the samples are placed at one side of an integrating sphere that is connected to a CCD-array spectrometer (Ocean Optics). The samples were illuminated by a laser with a wavelength of 532 nm. The illumination spot had an area of 0.12 cm^2, and the photon flux was $1.2 \cdot 10^{16}$ photons s^{-1} (≈1-Sun equivalent). The samples were illuminated from the substrate side.

Setup 2: For PL measurements of solar cell partial stacks in N_2 atmosphere, a prototype of the "LuQY Pro" setup by QYB in a glovebox was used. In this setup, a 532 nm wavelength laser was directed over a parabolic mirror onto the sample. The PL from the sample was collected over two serial plano-convex lenses via a fiber to a spectrometer (QE Pro, Ocean Insight). The signal was compiled using software by Quantum Yield Berlin (QYB). The laser (Insaneware) had an excitation fluence of approximately 1-Sun equivalent and illuminated an area of 0.14 cm^2 on the sample. The samples were illuminated from the substrate side.

The calculation of the QFLS was estimated from the generalized Planck law using the high-energy tail method.[78]

Setup 3: For steady-state PL measurements at different O_2 and air pressures, an Edinburgh FLS980 spectrometer was used. The excitation wavelength was 510 nm. The samples were mounted in a sealed chamber, in which the pressure of different working gases could be controlled between 0.05 mbar to 1 bar. For each pressure, the PL emission was averaged over the emission at the three wavelengths at/around the peak emission over 10 scans. The partial pressure of O_2 in air was calculated under the assumption of an ideal gas with an O_2 concentration of 21%$_{mol}$. For measurements with pure O_2, an "Oxygen N48" gas bottle from Air Liquide (<2 ppmv of water and <0.2 ppm-mol of KW, CO, and CO_2) was used.

Setup 4: For PL measurements of C_{60} thin films, the sample was placed in an air-tight chamber under a nitrogen atmosphere inside a glovebox. The chamber was then mounted on an optical table and connected to a vacuum pump. The sample was illuminated using a 445 nm continuous laser focused onto the C_{60} layer. Emission spectra were continuously recorded using an Andor Solis 803 system equipped with a silicon detector. Spectra were collected every 2.1 s, with each acquisition using an exposure time of 0.5 s and averaging four accumulations. Initially, the samples were held at atmospheric pressure in a nitrogen environment. Subsequently, the vacuum pump was activated, reducing the chamber pressure to 1×10^{-3} torr. Once the desired vacuum pressure was achieved, the pump was turned off, and the chamber was vented to air while the PL emission was tracked.

Transient Photoluminescence (trPL): Setup 1: The measurements for the results shown in Figure 1b were performed with a home-built confocal PL setup in air on encapsulated samples. The setup featured an "80:20"-"transmission:reflection"-beam splitter to separate the excitation and detection paths. A 700 nm diode laser (IB-705-B laser head with Taiko driver, Picoquant) with a pulse duration of ≈100 ps and a repetition rate of 10 kHz was used for excitation from the substrate side. The laser beam was passed through a cleanup filter (FF01-700/13–25, Semrock), and the energy of the laser beam was tuned by a linear-gradient neutral density filter to ≈0.2 µW (≈0.8 µW readout on power meter). An off-axis parabolic mirror with a 5 cm focal length has been used for the focus and PL collection. The laser spot size is a circle with a ≈250 µm diameter. A silicon single-photon avalanche diode (Laser Components COUNT50) has been employed for the PL detection, and the signal was cut by a 715 nm long-pass filter (FF01-715/LP-25, Semrock). The PL count and decay histogram were recorded by a TimeHarp260 Nano time-correlated single photon counting module (Picoquant).

Setup 2: For the results represented in Figure S4 (Supporting Information), second setup was used. Here, the sample was photoexcited by a pulsed femtosecond laser with a wavelength of 515 nm, a pulse length of 400 fs, a repetition rate of 20 kHz, and a beam diameter of 3 mm. The light intensity is adjusted by reflective neutral density filters. The incident light intensity (W cm^{-2}) was measured by a power meter to which a pinhole with a diameter of 0.5 mm was attached. The laser light is suppressed by a 550 nm long pass and a 50 nm bandpass centered at 750 nm. The trPL was measured by a single photon counting system from PicoQuant PMA Hybrid Series.

The decay curve was fitted by an arbitrary sum of exponential slopes to compute the differential lifetime. The differential lifetime was calculated via:[49]

$$\tau_{diff} = -\left[\frac{d\left(ln\left(trPL\left(t\right)\right)\right)}{dt}\right]^{-1} \quad (1)$$

For differential lifetime plots, one has to estimate the QFLS. For this, three relations were used:

$$PL = k_{rad} np = k_{rad} n^2 \quad (2)$$

$$QFLS = kTln\left(\frac{PL}{PL\left(0\right)}\right) + kTln\left(\frac{n(0)^2}{n_i^2}\right) with \;\; n_i^2 = N_c N_v e^{\frac{-E_g}{kT}} \quad (3)$$

With the assumption of $N_c = N_v = 2 \cdot 10^{18}$ cm^{-3}. This value determines the starting QFLS(0). The other values are determined by the normalized PL decay PL/PL(0), respectively.

Transient Surface Photovoltage (trSPV): Transient surface photovoltage (trSPV) measurements were carried out on an in-house-built setup. The samples were laser-excited from the encapsulation glass side with a tunable pumped pulse laser (Nd:YAG Laser, EKSPLA, NT230-50-SH/SF-SCU-2H). For the measurements in this work, excitation energies between 1.4 and 3.0 eV and a pulse time of 3–6 ns at a frequency of 2 Hz were used. The laser fluence was controlled via neutral density filters and adjusted to yield charge carrier densities equivalent to 1 Sun. For measurements at high illumination intensities, as shown in Figure S6 (Supporting Information), no filters were used yielding charge carrier densities equivalent to >100 Suns. A total of 20 curves were recorded and averaged. The transients were measured with an oscilloscope card (Gage, CSE 1622- 4GS, 200 MS s^{-1}) using an in-house developed for logarithmic read-out.

Current Density–Voltage Measurement (J–V): Current density–voltage (*J–V*) characteristics of perovskite single-junction solar cells were conducted in N_2 atmosphere and under 1-Sun AM1.5g equivalent illumination (1000 W m^{-2}) from an Oriel LCS-100 class ABB sun simulator. The illumination intensity was calibrated to the J_{SC} of the KG3 filtered silicon reference cell calibrated by Fraunhofer ISE CalLab. For obtaining the *J–V* scans, the voltage was swept in reverse (V_{OC} to J_{SC}) and forward direction (J_{SC} to V_{OC}) between 1.3 and −0.02 V in 0.02 V steps and with an integration time of 20 ms and a settling time of 20 ms. The scans were recorded by a Keithley 2400 digital source measure unit, which was controlled by custom LabView software and used a two-wire arrangement. The devices were kept at a constant temperature of 25 °C.

Long-Term Stability Measurement: Measurements were conducted with a custom-built high-throughput ageing setup as described in ref.[79]. A perturb-and-observe-algorithm[80] with a delay time of 1 s and a voltage step-width of 0.01 V was applied to each cell individually, and the MPP merits updated every 2 min. 1-Sun-equivalent illumination was provided by a metal-halide lamp using an H6 filter, with the intensity actively controlled with an irradiation sensor calibrated with a KG3-filtered silicon reference cell. The device temperature of 25 °C was controlled by Peltier elements using heat pads for direct thermal coupling.

Photoelectron Spectroscopy (PES): X-ray photoelectron spectroscopy (XPS) and UV photoelectron spectroscopy (UPS) were performed in an ultra-high vacuum (UHV) system (base pressure $<10^{-10}$ mbar) by SPECS Surface Nano Analysis GmbH. Via an inert transfer, the samples were directly loaded into a glovebox attached to UHV. To ensure a minimal impact of the UHV condition on potential desorption of O_2 or H_2O and hence influence on the sample surface condition, the samples were loaded one by one, and each was measured as quickly as possible (<20 min) after loading.

As it is the most surface sensitive, the first UPS with He-I ($h\nu = 21.2$ eV) were performed, with a survey scan followed by a more detailed scan of the highest occupied molecular orbital (HOMO) region and a control survey scan. Throughout the measurement time between the first and the control survey a rigid shift of the spectrum (to lower work function and higher HOMO position) was observed, which was in the range of 10–30 meV and, thus, much lower than the observed trends using the different gas treatments. A hemispheric electron analyzer (PHOIBOS150) with a 1D-DLD detector was used with a pass energy of 2.25 eV in low angular diffraction lens mode with entrance slit 0.8 × 20c, an open exit slit and a bias voltage between the detector and the exit slit of −0.5 V. To investigate the secondary electron cut-off (SECO), a bias voltage between the sample and the analyzer of -7 V was applied.

The SECO was evaluated by the center of a sigmoidal Boltzmann function, whereas the HOMO edge was obtained by a linear extrapolation of the leading edge of the HOMO and the intercept with the background signal. The spectra were corrected for the appearance of satellite features in the HOMO/bandgap region beforehand. The observed shifts of the HOMO edge were confirmed by the same shift being observed for the HOMO peak.

XPS measurements were performed using Al-K_α excitation (1486.6 eV) with 14 kV and 300 W and a pass energy of 30 eV for the detailed spectra and 60 eV for the survey spectrum. A hemispheric electron analyzer (PHOIBOS150 1D-DLD) was used in medium area lens mode with entrance slit 7 × 20c and a bias voltage between the detector and the exit slit of 35 V. To ensure a homogeneous distribution of the analyzer bias voltage, a mesh was chosen as exit slit of the analyzer.

Kelvin Probe (KP) Measurements: KP measurements were performed using a custom-built KP consisting of a vibrating gold mesh driven by a piezo electric crystal (KP and contact potential difference (CPD) controller by Besocke Delta Phi). For the measurements, a bias voltage of 5 V was applied. The measurements were conducted in vacuum (0.001 mbar), N_2 (1 bar), and ambient air (1 bar). The work function of the sample φ^{sample} was calculated using the following equation:

$$\varphi^{\text{sample}} = eV_{\text{CPD}}^{\text{sample}} + \varphi^{\text{HOPG}} - eV_{\text{CPD}}^{\text{HOPG}} \quad (4)$$

The stabilized CPD values (V_{CPD}) of highly oriented pyrolytic graphite (HOPG) and the sample were averaged over at least 300 s. For the work function of HOPG φ^{HOPG}, a literature value of 4.475 eV was assumed.[81]

Contact Angle Measurements: A Krüss 100S drop shape analyzer was used to perform contact angle measurements based on the sessile drop method on solar cell partial stacks fabricated on glass/ITO substrates. The measurements were conducted at room temperature in air and using two different liquids, i.e., water as a polar liquid and diiodo-methane as a highly dispersive liquid. The contact angle for both liquids was determined as the arithmetic mean of at least two measurements on the same sample. The surface free energy and respective disperse and polar parts for each sample were calculated based on the mean contact angles with water and diiodo-methane using the Owens–Wendt–Rabel-Kaelble (OWRK) method.[74,75]

Scanning Electron Microscopy (SEM): Top-view SEM measurements of solar cell partial stacks were performed using a Zeiss Merlin Field Emission SEM with a Gemini 2 optical column equipped with an InLens detector for secondary electrons. An acceleration voltage of 5 kV and magnification of 80 K were used for all images.

Ultraviolet–visible-near-infrared (UV–Vis–NIR) spectroscopy: A Perkin Elmer Lambda 1050+ spectrophotometer was used to obtain the optical properties of encapsulated solar cell partial stacks. Measurements were performed in ambient air in a wavelength range between 300 and 1200 nm with a 5 nm increment.

Supporting Information

Supporting Information is available from the Wiley Online Library or from the author.

Acknowledgements

The authors thank J. Beckedahl, M. Choyne., C. Ferber, M. Wittig, T. Lußky, and H. Heinz for the technical support in HySPRINT Helmholtz Innovation Lab. The authors thank M. Rusu for the insightful discussions,

L. J. Affonço for technical support with contact angle measurements, O. Karalis for the support with transient PL measurements, and T. Dittrich for the technical assistance and expert support with KP measurements. The authors thank for funding from the Helmholtz Association within the HySPRINT Innovation lab project, the EU partnering project "TAPAS," and the project "Zeitenwende–Zukunftstechnologie Tandem–Solarzellen," as well as the HyPerCells research school. The authors acknowledge funding from the project "SHAPE" funded by the Federal Ministry of Economy and Climate Action (BMWK) (grant no. 03EE1123CC) and the project "Supertandem" funded by the European Union's Horizon Europe research and innovation program (grant no. 101075605).

Open access funding enabled and organized by Projekt DEAL.

Conflict of Interest

The authors declare no conflict of interest.

Data Availability Statement

The data that support the findings of this study are available from the corresponding author upon reasonable request.

Keywords

C_{60}, non-radiative recombination, oxygen, perovskite solar cells, SnO_x

Received: March 4, 2025
Revised: April 15, 2025
Published online: May 6, 2025

[1] Z. Fang, B. Deng, Y. Jin, L. Yang, L. Chen, Y. Zhong, H. Feng, Y. Yin, K. Liu, Y. Li, J. Zhang, J. Huang, Q. Zeng, H. Wang, X. Yang, J. Yang, C. Tian, L. Xie, Z. Wei, X. Xu, *Nat. Commun.* **2024**, *15*, 10554.

[2] S. Mariotti, E. Köhnen, F. Scheler, K. Sveinbjörnsson, L. Zimmermann, M. Piot, F. Yang, B. Li, J. Warby, A. Musiienko, D. Menzel, F. Lang, S. Keßler, I. Levine, D. Mantione, A. Al-Ashouri, M. S. Härtel, K. Xu, A. Cruz, J. Kurpiers, P. Wagner, H. Köbler, J. Li, A. Magomedov, D. Mecerreyes, E. Unger, A. Abate, M. Stolterfoht, B. Stannowski, R. Schlatmann, et al., *Science* **2023**, *381*, 63.

[3] E. Aydin, E. Ugur, B. K. Yildirim, T. G. Allen, P. Dally, A. Razzaq, F. Cao, L. Xu, B. Vishal, A. Yazmaciyan, A. A. Said, S. Zhumagali, R. Azmi, M. Babics, A. Fell, C. Xiao, S. De Wolf, *Nature* **2023**, *623*, 732.

[4] X. Y. Chin, D. Turkay, J. A. Steele, S. Tabean, S. Eswara, M. Mensi, P. Fiala, C. M. Wolff, A. Paracchino, K. Artuk, D. Jacobs, Q. Guesnay, F. Sahli, G. Andreatta, M. Boccard, Q. Jeangros, C. Ballif, *Science* **2023**, *381*, 59.

[5] E. Ugur, A. A. Said, P. Dally, S. Zhang, C. E. Petoukhoff, D. Rosas-Villalva, S. Zhumagali, B. K. Yildirim, A. Razzaq, S. Sarwade, A. Yazmaciyan, D. Baran, F. Laquai, C. Deger, I. Yavuz, T. G. Allen, E. Aydin, S. De Wolf, *Science* **2024**, *385*, 533.

[6] Y. Wang, R. Lin, C. Liu, X. Wang, C. Chosy, Y. Haruta, A. D. Bui, M. Li, H. Sun, X. Zheng, H. Luo, P. Wu, H. Gao, W. Sun, Y. Nie, H. Zhu, K. Zhou, H. T. Nguyen, X. Luo, L. Li, C. Xiao, M. I. Saidaminov, S. D. Stranks, L. Zhang, H. Tan, *Nature* **2024**, *635*, 867.

[7] H. Chen, C. Liu, J. Xu, A. Maxwell, W. Zhou, Y. Yang, Q. Zhou, A. S. R. Bati, H. Wan, Z. Wang, L. Zeng, J. Wang, P. Serles, Y. Liu, S. Teale, Y. Liu, M. I. Saidaminov, M. Li, N. Rolston, S. Hoogland, T. Filleter, M. G. Kanatzidis, B. Chen, Z. Ning, E. H. Sargent, *Science* **2024**, *384*, 189.

[8] D. Yu, M. Pan, G. Liu, X. Jiang, X. Wen, W. Li, S. Chen, W. Zhou, H. Wang, Y. Lu, M. Ma, Z. Zang, P. Cheng, Q. Ji, F. Zheng, Z. Ning, *Nat. Energy* **2024**, *9*, 298.

[9] S. Liu, Y. Lu, C. Yu, J. Li, R. Luo, R. Guo, H. Liang, X. Jia, X. Guo, Y.-D. Wang, Q. Zhou, X. Wang, S. Yang, M. Sui, P. Müller-Buschbaum, Y. Hou, *Nature* **2024**, *628*, 306.

[10] F. Xu, E. Aydin, J. Liu, E. Ugur, G. T. Harrison, L. Xu, B. Vishal, B. K. Yildirim, M. Wang, R. Ali, A. S. Subbiah, A. Yazmaciyan, S. Zhumagali, W. Yan, Y. Gao, Z. Song, C. Li, S. Fu, B. Chen, A. ur Rehman, M. Babics, A. Razzaq, M. De Bastiani, T. G. Allen, U. Schwingenschlögl, Y. Yan, F. Laquai, E. H. Sargent, S. De Wolf, *Joule* **2024**, *8*, 224.

[11] S. Hu, J. Wang, P. Zhao, J. Pascual, J. Wang, F. Rombach, A. Dasgupta, W. Liu, M. A. Truong, H. Zhu, M. Kober-Czerny, J. N. Drysdale, J. A. Smith, Z. Yuan, G. J. W. Aalbers, N. R. M. Schipper, J. Yao, K. Nakano, S.-H. Turren-Cruz, A. Dallmann, M. G. Christoforo, J. M. Ball, D. P. McMeekin, K.-A. Zaininger, Z. Liu, N. K. Noel, K. Tajima, W. Chen, M. Ehara, R. A. J. Janssen, et al., *Nature* **2024**, *639*, 93.

[12] J. Liu, Y. He, L. Ding, H. Zhang, Q. Li, L. Jia, J. Yu, T. W. Lau, M. Li, Y. Qin, X. Gu, F. Zhang, Q. Li, Y. Yang, S. Zhao, X. Wu, J. Liu, T. Liu, Y. Gao, Y. Wang, X. Dong, H. Chen, P. Li, T. Zhou, M. Yang, X. Ru, F. Peng, S. Yin, M. Qu, D. Zhao, et al., *Nature* **2024**, *635*, 596.

[13] J. Siekmann, A. Kulkarni, S. Akel, B. Klingebiel, M. Saliba, U. Rau, T. Kirchartz, *Adv. Energy Mater.* **2023**, *13*, 2300448.

[14] Z. Guan, Y. Li, P. Man, H. Tan, Q. Wei, J. Liu, M. Li, T. H. Ly, J. Yin, C.-S. Lee, *Adv. Mater.* **2024**, *36*, 2407406.

[15] A. A. Said, E. Aydin, E. Ugur, Z. Xu, C. Deger, B. Vishal, A. Vlk, P. Dally, B. K. Yildirim, R. Azmi, J. Liu, E. A. Jackson, H. M. Johnson, M. Gui, H. Richter, A. R. Pininti, H. Bristow, M. Babics, A. Razzaq, T. G. Allen, M. Ledinský, I. Yavuz, B. P. Rand, S. De Wolf, *Nat. Commun.* **2024**, *15*, 708.

[16] J. Warby, F. Zu, S. Zeiske, E. Gutierrez-Partida, L. Frohloff, S. Kahmann, K. Frohna, E. Mosconi, E. Radicchi, F. Lang, S. Shah, F. Peña-Camargo, H. Hempel, T. Unold, N. Koch, A. Armin, F. De Angelis, S. D. Stranks, D. Neher, M. Stolterfoht, *Adv. Energy Mater.* **2022**, *12*, 2103567.

[17] D. Menzel, A. Al-Ashouri, A. Tejada, I. Levine, J. A. Guerra, B. Rech, S. Albrecht, L. Korte, *Adv. Energy Mater.* **2022**, *12*, 2201109.

[18] F. Ye, S. Zhang, J. Warby, J. Wu, E. Gutierrez-Partida, F. Lang, S. Shah, E. Saglamkaya, B. Sun, F. Zu, S. Shoaee, H. Wang, B. Stiller, D. Neher, W.-H. Zhu, M. Stolterfoht, Y. Wu, *Nat. Commun.* **2022**, *13*, 7454.

[19] C. Liu, Y. Yang, H. Chen, J. Xu, A. Liu, A. Bati, H. Zhu, L. Grater, B. Chen, M. Kanatzidis, E. Sargent, *Science* **2023**, *382*, 810.

[20] Q. Jiang, J. Tong, Y. Xian, R. A. Kerner, S. P. Dunfield, C. Xiao, R. A. Scheidt, D. Kuciauskas, X. Wang, M. P. Hautzinger, R. Tirawat, M. C. Beard, D. P. Fenning, J. J. Berry, B. W. Larson, Y. Yan, K. Zhu, *Nature* **2022**, *611*, 278.

[21] H. Chen, A. Maxwell, C. Li, S. Teale, B. Chen, T. Zhu, E. Ugur, G. Harrison, L. Grater, J. Wang, Z. Wang, L. Zeng, S. M. Park, L. Chen, P. Serles, R. A. Awni, B. Subedi, X. Zheng, C. Xiao, N. J. Podraza, T. Filleter, C. Liu, Y. Yang, J. M. Luther, S. De Wolf, M. G. Kanatzidis, Y. Yan, E. H. Sargent, *Nature* **2023**, *613*, 676.

[22] S. Hu, J. Pascual, W. Liu, T. Funasaki, M. A. Truong, S. Hira, R. Hashimoto, T. Morishita, K. Nakano, K. Tajima, R. Murdey, T. Nakamura, A. Wakamiya, *ACS Appl. Mater. Interfaces* **2022**, *14*, 56290.

[23] Z. Liu, H. Li, Z. Chu, R. Xia, J. Wen, Y. Mo, H. Zhu, H. Luo, X. Zheng, Z. Huang, X. Luo, B. Wang, X. Zhang, G. Yang, Z. Feng, Y. Chen, W. Kong, J. Gao, H. Tan, *Adv. Mater.* **2024**, *36*, 2308370.

[24] R. Azmi, D. S. Utomo, B. Vishal, S. Zhumagali, P. Dally, A. M. Risqi, A. Prasetio, E. Ugur, F. Cao, I. F. Imran, A. A. Said, A. R. Pininti, A. S. Subbiah, E. Aydin, C. Xiao, S. I. Seok, S. De Wolf, *Nature* **2024**, *628*, 93.

[25] E. Ugur, E. Aydin, M. D. Bastiani, G. T. Harrison, B. K. Yildirim, S. Teale, B. Chen, J. Liu, M. Wang, A. Seitkhan, M. Babics, A. S. Subbiah, A. A. Said, R. Azmi, A. ur Rehman, T. G. Allen, P. Schulz, E. H. Sargent, F. Laquai, S. D. Wolf, *Matter* **2023**, *6*, 2919.

[26] A. Al-Ashouri, E. Köhnen, B. Li, A. Magomedov, H. Hempel, P. Caprioglio, J. Marquez-Prieto, A. Vilches, E. Kasparavičius, J. Smith, N. Phung, D. Menzel, M. Grischek, L. Kegelmann, D. Skroblin, C. Gollwitzer, T. Malinauskas, M. Jošt, G. Matič, S. Albrecht, *Science* **2020**, *370*, 1300.
[27] J. Liu, M. De Bastiani, E. Aydin, G. T. Harrison, Y. Gao, R. R. Pradhan, M. K. Eswaran, M. Mandal, W. Yan, A. Seitkhan, M. Babics, A. S. Subbiah, E. Ugur, F. Xu, L. Xu, M. Wang, A. ur Rehman, A. Razzaq, J. Kang, R. Azmi, A. A. Said, F. H. Isikgor, T. G. Allen, D. Andrienko, U. Schwingenschlögl, F. Laquai, S. De Wolf, *Science* **2022**, *377*, 302.
[28] K. Artuk, D. Turkay, M. D. Mensi, J. A. Steele, D. A. Jacobs, M. Othman, X. Yu Chin, S.-J. Moon, A. N. Tiwari, A. Hessler-Wyser, Q. Jeangros, C. Ballif, C. M. Wolff, *Adv. Mater.* **2024**, *36*, 2311745.
[29] J. W. Arbogast, A. P. Darmanyan, C. S. Foote, F. N. Diederich, R. L. Whetten, Y. Rubin, M. M. Alvarez, S. J. Anz, *J. Phys. Chem.* **1991**, *95*, 11.
[30] M. Orfanopoulos, *Photochem. Photobiol.* **2021**, *97*, 1182.
[31] K. Kawaoka, A. U. Khan, D. R. Kearns, *J. Chem. Phys.* **1967**, *46*, 1842.
[32] T. Konishi, M. Fujitsuka, O. Ito, *Chem. Lett.* **2000**, *29*, 202.
[33] J. Lee, J. D. Fortner, J. B. Hughes, J.-H. Kim, *Environ. Sci. Technol.* **2007**, *41*, 2529.
[34] Y. Yamakoshi, N. Umezawa, A. Ryu, K. Arakane, N. Miyata, Y. Goda, T. Masumizu, T. Nagano, *J. Am. Chem. Soc.* **2003**, *125*, 12803.
[35] J. P. Bastos, E. Voroshazi, E. Fron, G. Brammertz, T. Vangerven, M. Van der Auweraer, J. Poortmans, D. Cheyns, *ACS Appl. Mater. Interfaces* **2016**, *8*, 9798.
[36] T. Matsushima, M. Yahiro, C. Adachi, *Appl. Phys. Lett.* **2007**, *91*, 103505.
[37] M. Rusu, J. Strotmann, M. Vogel, M. Ch Lux-Steiner, K. Fostiropoulos, *Appl. Phys. Lett.* **2007**, *90*, 153511.
[38] A. Tapponnier, I. Biaggio, P. Günter, *Appl. Phys. Lett.* **2005**, *86*, 112114.
[39] Y. Tanaka, K. Kanai, Y. Ouchi, K. Seki, *Chem. Phys. Lett.* **2007**, *441*, 63.
[40] L. Tsetseris, S. T. Pantelides, *Phys. Rev. B* **2010**, *82*, 045201.
[41] C. H. Lee, G. Yu, B. Kraabel, D. Moses, V. I. Srdanov, *Phys. Rev. B* **1994**, *49*, 10572.
[42] R. Könenkamp, G. Priebe, B. Pietzak, *Phys. Rev. B* **1999**, *60*, 11804.
[43] A. G. Kuba, C. Santiwipharat, R. J. Richardson, U. K. Das, K. D. Dobson, W. N. Shafarman, *ACS Appl. Energy Mater.* **2024**, *7*, 11921.
[44] F. Li, X. Deng, F. Qi, Z. Li, D. Liu, D. Shen, M. Qin, S. Wu, F. Lin, S.-H. Jang, J. Zhang, X. Lu, D. Lei, C.-S. Lee, Z. Zhu, A. K.-Y. Jen, *J. Am. Chem. Soc.* **2020**, *142*, 20134.
[45] E. R. Nandayapa, K. Hirselandt, C. Boeffel, E. L. Unger, E. J. W. List-Kratochvil, *Adv. Opt. Mater.* **2021**, *9*, 2101825.
[46] Y. Tian, M. Peter, E. Unger, M. Abdellah, K. Zheng, T. Pullerits, A. Yartsev, V. Sundström, I. G. Scheblykin, *Phys. Chem. Chem. Phys.* **2015**, *17*, 24978.
[47] R. Brenes, C. Eames, V. Bulović, M. S. Islam, S. D. Stranks, *Adv. Mater.* **2018**, *30*, 1706208.
[48] Z. Zhang, Y. Liu, P. Zhang, Y. Mao, *Org. Electron.* **2021**, *88*, 106007.
[49] Y. Yuan, G. Yan, C. Dreessen, T. Rudolph, M. Hülsbeck, B. Klingebiel, J. Ye, U. Rau, T. Kirchartz, *Nat. Mater.* **2024**, *23*, 391.
[50] W. Shockley, W. T. Read, *Phys. Rev.* **1952**, *87*, 835.
[51] E. Gutierrez-Partida, M. Rusu, F. Zu, M. Raoufi, J. Diekmann, N. Tokmoldin, J. Warby, D. Menzel, F. Lang, S. Shah, S. Shoaee, L. Korte, T. Unold, N. Koch, T. Kirchartz, D. Neher, M. Stolterfoht, *ACS Appl. Mater. Interfaces* **2025**, *17*, 11176.
[52] L. Canil, T. Cramer, B. Fraboni, D. Ricciarelli, D. Meggiolaro, A. Singh, M. Liu, M. Rusu, C. M. Wolff, N. Phung, Q. Wang, D. Neher, T. Unold, P. Vivo, A. Gagliardi, F. D. Angelis, A. Abate, *Energy Environ. Sci.* **2021**, *14*, 1429.
[53] A. M. Rao, K.-A. Wang, J. M. Holden, Y. Wang, P. Zhou, P. C. Eklund, C. C. Eloi, J. D. Robertson, *J. Mater. Res.* **1993**, *8*, 2277.
[54] H. Werner, T. Schedel-Niedrig, M. Wohlers, D. Herein, B. Herzog, R. Schlögl, M. Keil, A. M. Bradshaw, J. Kirschner, *J. Chem. Soc. Faraday Trans.* **1994**, *90*, 403.
[55] P. C. Eklund, A. M. Rao, P. Zhou, Y. Wang, J. M. Holden, *Thin Solid Films* **1995**, *257*, 185.
[56] A. Hamed, Y. Y. Sun, Y. K. Tao, R. L. Meng, P. H. Hor, *Phys. Rev. B* **1993**, *47*, 10873.
[57] H. Habuchi, S. Nitta, D. Han, S. Nonomura, *J. Appl. Phys.* **2000**, *87*, 8580.
[58] O. P. Dmytrenko, N. P. Kulish, Y.u. I. Prylutskyy, T. V. Rodionova, T. D. Shatniy, U. Ritter, L. Carta-Abelmann, P. Scharff, T. Braun, *Thin Solid Films* **2008**, *516*, 7937.
[59] R. Antoine, P.h. Dugourd, D. Rayane, E. Benichou, M. Broyer, F. Chandezon, C. Guet, *J. Chem. Phys.* **1999**, *110*, 9771.
[60] P. A. Gravil, P.h. Lambin, G. Gensterblum, L. Henrard, P. Senet, A. A. Lucas, *Surf. Sci.* **1995**, *329*, 199.
[61] T. Kirchartz, T. Markvart, U. Rau, D. A. Egger, *J. Phys. Chem. Lett.* **2018**, *9*, 939.
[62] R. A. Assink, J. E. Schirber, D. A. Loy, B. Morosin, G. A. Carlson, *J. Mater. Res.* **1992**, *7*, 2136.
[63] E. T. Hoke, I. T. Sachs-Quintana, M. T. Lloyd, I. Kauvar, W. R. Mateker, A. M. Nardes, C. H. Peters, N. Kopidakis, M. D. McGehee, *Adv. Energy Mater.* **2012**, *2*, 1351.
[64] V. N. Denisov, B. N. Mavrin, A. A. Zakhidov, G. Ruani, R. Zamboni, C. Taliani, *Synth. Met.* **1993**, *56*, 3119.
[65] Y. Dong, F. M. Rombach, G. Min, H. J. Snaith, C.-T. Lin, S. A. Haque, T. J. Macdonald, *Mater. Sci. Eng. R Rep.* **2025**, *162*, 100875.
[66] E. Köhnen, M. Jošt, A. B. Morales-Vilches, P. Tockhorn, A. Al-Ashouri, B. Macco, L. Kegelmann, L. Korte, B. Rech, R. Schlatmann, B. Stannowski, S. Albrecht, *Sustain. Energy Fuels* **2019**, *3*, 1995.
[67] B. Yu, F. Tang, Y. Yang, J. Huang, S. Wu, F. Lu, W. Duan, A. Lambertz, K. Ding, Y. Mai, *Adv. Mater.* **2023**, *35*, 2202447.
[68] J. A. Raiford, C. C. Boyd, A. F. Palmstrom, E. J. Wolf, B. A. Fearon, J. J. Berry, M. D. McGehee, S. F. Bent, *Adv. Energy Mater.* **2019**, *9*, 1902353.
[69] K. O. Brinkmann, J. Zhao, N. Pourdavoud, T. Becker, T. Hu, S. Olthof, K. Meerholz, L. Hoffmann, T. Gahlmann, R. Heiderhoff, M. F. Oszajca, N. A. Luechinger, D. Rogalla, Y. Chen, B. Cheng, T. Riedl, *Nat. Commun.* **2017**, *8*, 13938.
[70] S. A. Johnson, K. P. White, J. Tong, S. You, A. Magomedov, B. W. Larson, D. Morales, R. Bramante, E. Dunphy, R. Tirawat, C. L. Perkins, J. Werner, G. Lahti, C. Velez, M. F. Toney, K. Zhu, M. D. McGehee, J. J. Berry, A. F. Palmstrom, *Joule* **2023**, *7*, 2873.
[71] Z. Xiong, L. Wu, X. Zhou, S. Yang, Z. Liu, W. Liu, J. Zhao, W. Li, C. Yu, K. Yao, *Small* **2024**, *20*, 2308024.
[72] N. Ren, C. Zhu, R. Li, S. Mazumdar, C. Sun, B. Chen, Q. Xu, P. Wang, B. Shi, Q. Huang, S. Xu, T. Li, Y. Zhao, X. Zhang, *Appl. Phys. Lett.* **2022**, *121*, 033502.
[73] K. A. Bush, A. F. Palmstrom, Z. J. Yu, M. Boccard, R. Cheacharoen, J. P. Mailoa, D. P. McMeekin, R. L. Z. Hoye, C. D. Bailie, T. Leijtens, I. M. Peters, M. C. Minichetti, N. Rolston, R. Prasanna, S. Sofia, D. Harwood, W. Ma, F. Moghadam, H. J. Snaith, T. Buonassisi, Z. C. Holman, S. F. Bent, M. D. McGehee, *Nat. Energy* **2017**, *2*, 17009.
[74] A. Rudawska, E. Jacniacka, *Int. J. Adhes. Adhes.* **2009**, *29*, 451.
[75] D. Y. Kwok, A. W. Neumann, *Adv. Colloid Interface Sci.* **1999**, *81*, 167.
[76] I. L. Repins, M. Owen-Bellini, M. D. Kempe, M. G. Deceglie, J. J. Berry, N. Y. Doumon, T. J. Silverman, L. T. Schelhas, *Cell Rep. Phys. Sci.* **2024**, *5*, 101969.
[77] A. Al-Ashouri, M. Marčinskas, E. Kasparavičius, T. Malinauskas, A. Palmstrom, V. Getautis, S. Albrecht, M. D. McGehee, A. Magomedov, *ACS Energy Lett.* **2023**, *8*, 898.

[78] T. Unold, L. Gütay, in *Adv. Charact. Tech. Thin Film Sol. Cells*, Wiley-VCH, Weinheim, Germany **2016**, 275.
[79] H. Köbler, S. Neubert, M. Jankovec, B. Glažar, M. Haase, C. Hilbert, M. Topič, B. Rech, A. Abate, *Energy Technol.* **2022**, *10*, 2200234.
[80] L. Rakocevic, F. Ernst, N. T. Yimga, S. Vashishtha, T. Aernouts, T. Heumueller, C. J. Brabec, R. Gehlhaar, J. Poortmans, *Sol. RRL* **2019**, *3*, 1800287.
[81] W. N. Hansen, G. J. Hansen, *Surf. Sci.* **2001**, *481*, 172.